J. Am. Soc. Mass Spectrom. (2016) 27:1419–1428
DOI: 10.1007/s13361-016-1414-0

RESEARCH ARTICLE

Probing the Relationship Between Detected Ion Intensity, Laser Fluence, and Beam Profile in Thin Film and Tissue in MALDI MSI

Rory T. Steven,[1] Alan M. Race,[1] Josephine Bunch[1,2]

[1]National Centre of Excellence in Mass Spectrometry Imaging (NiCE-MSI), National Physical Laboratory (NPL), Teddington, TW11 0LW, UK
[2]School of Pharmacy, University of Nottingham, Nottingham, NG7 2RD, UK

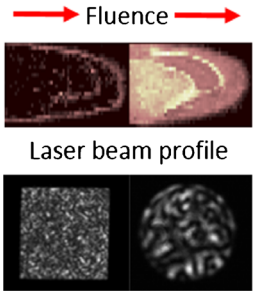

Abstract. Matrix assisted laser desorption ionization mass spectrometry imaging (MALDI MSI) is increasingly widely used to provide information regarding molecular location within tissue samples. The nature of the photon distribution within the irradiated region, the laser beam profile, and fluence, will significantly affect the form and abundance of the detected ions. Previous studies into these phenomena have focused on circular-core optic fibers or Gaussian beam profiles irradiating dried droplet preparations, where peptides were employed as the analyte of interest. Within this work, we use both round and novel square core optic fibers of 100 and 50 μm diameter to deliver the laser photons to the sample. The laser beam profiles were recorded and analyzed to quantify aspects of the photon distributions and their relation to the spectral data obtained with each optic fiber. Beam profiles with a relatively small number of large beam profile features were found to give rise to the lowest threshold fluence. The detected ion intensity versus fluence relationship was investigated, for the first time, in both thin films of α-cyano-4-hydroxycinnamic acid (CHCA) with phosphatidylcholine (PC) 34:1 lipid standard and in CHCA coated murine tissue sections for both the square and round optic fibers in continuous raster imaging mode. The fluence threshold of ion detection was found to occur at between ~14 and ~64 J/m^2 higher in tissue compared with thin film for the same lipid, depending upon the optic fiber employed. The image quality is also observed to depend upon the fluence employed during image acquisition.

Keywords: MALDI MSI, Fluence, Laser beam profile, Lipid, Mass Spectrometry Imaging

Received: 20 November 2015/Revised: 14 April 2016/Accepted: 23 April 2016/Published Online: 20 May 2016

Introduction

Ablation and detected ion intensity in MALDI MS is known to have a strong dependence upon the laser energy per pulse and the size of this irradiated region, usually reported as the laser fluence (J/m^2). A threshold fluence of ion detection is typically reported as being between ~ 20 and 1700 J/m^2. The threshold energy and the effect of fluence on the detected ion intensity are also observed to depend upon the size of the irradiated area [1–3]. Beyond threshold energy, the rapid conversion of photons into heat leads to the creation of sub-surface nucleation, pressure waves, and subsequent molecule cluster and particle ejection [4, 5]. These effects bring with them a rapid increase in the detected ion intensity, typically described as the power law function, $I \alpha H^m$, where I is the detected ion intensity, H the fluence, and m the fitting parameter [3, 4, 6]. At fluences exceeding this regime of rapid increase, a plateau and eventual decrease in ion intensity is often observed. Typically it is expected that laser energies at or just past this plateau deliver the most useful data and so a laser energy of approximately two to three times the threshold fluence is usually recommended. It is important to note that this is likely to vary for particular matrix and sample system or instrumental setup [7]. More recently, a sigmoidal function has been reported for fitting to these data in an attempt to employ fitting parameters with a closer relation to physical phenomena such as the threshold energy for ion detection [7, 8].

Electronic supplementary material The online version of this article (doi:10.1007/s13361-016-1414-0) contains supplementary material, which is available to authorized users.

Correspondence to: Josephine Bunch; *e-mail:* Josephine.bunch@npl.co.uk

The effect of fluence on the detected ion intensity has been investigated by a number of groups for peptide and protein standards, e.g., substance P, with a range of matrices, e.g., 2,5-dihydroxybenzoic acid (2,5-DHB) or α-cyano-hydroxycin namic acid (CHCA) [2, 3, 7, 9]. There have not, however, been any similar investigations employing other analyte classes, such as lipids or drugs. Further to this, the implications for fluence response in more complex systems have not been studied in detail. Soltwisch et al. employed a combination of four peptides within their recent study [7], but no analysis of the effect of fluence on these molecules individually or of this increased complexity on the observed trends was explicitly presented. A 2006 study by the Korfmacher group showed the detected ion response to laser energy for clozapine and norclozapine in dosed rat brain tissue, but no measurement of the size of the irradiated area was carried out, nor was this performed in a spatially resolved (imaging) mode, meaning the spatial distribution of the drug within the tissue cannot be discounted as a significant contributor to the trends seen [10]. Lagarrigue et al. discussed the spectral differences resulting from different size irradiated areas and fluence regimes in a tissue imaging context but no energy measurements were presented to accompany these data [11]. Within laser ablation studies, it is known that the fluence employed when irradiating biological media dictates the amount of material removed and, therefore to a lesser extent, the detected spectral properties [12].

Commercially available MALDI MS instruments do not provide the ability for users to measure their laser energy and only provide relative percentage control of the energy per pulse employed. This is in contrast to the field of secondary ion mass spectrometry where the primary ion current, which serves a similar role to the laser in LDI MS type studies, is able to be measured and controlled precisely in many commercial instruments. The combination of the fluence dependence of detected ion intensity and the lack of study of this phenomenon in a MALDI MS tissue imaging context are therefore of great interest, particularly with the large and increasing number of MALDI MS tissue imaging publications each year where, typically, the researchers involved do not know the laser energy they are using in their experiments.

The laser beam profile is also an important factor within MALDI MS. This is not solely because it describes the area of the irradiated region but because the distribution of photons within the irradiated area will also influence the desorption and ablation process. The Ens group demonstrated that the different photon distribution, resulting from nitrogen and Nd:YAG lasers, give rise to different ion yields for substance P with CHCA [2]. This concept of some photon distributions being more optimal than others was then built upon by Holle et al. in the creation and study of 'structured' laser beam profiles, demonstrating that lower total energy could be used where a more optimal photon distribution is employed, to give rise to equivalent quality data [13]. Their study also showed that the apparent threshold energy of analyte ion detection can vary depending upon the beam profile photon distribution. It is important to note that these results were obtained from a large number of shots where the 'structured' beam profiles were deliberately altered to a new photon distribution for every shot. Regardless of this, there will certainly be a photon distribution that is most optimal for a given matrix type, crystal size, morphology, and distribution. To this end, a user-defined photon distribution may become an important consideration within MALDI MS using, for example, adaptive optics techniques to achieve an optimal beam profile [14].

Within this study, square and round core fiber optic patchcords of 50 and 100 μm core diameters are employed to deliver the laser to the sample. The use of two different fiber core shapes and diameters allows study of the novel beam profile resulting from square core fibers and also provides four different size irradiated areas for the study of the fluence response of detected ion intensity. This relationship is studied in continuous stage raster mode in thin film lipid standard (phosphatidylcholine (PC) 34:1) with CHCA as well as in CHCA coated murine brain tissue sections within a MALDI MSI context. Both of these sample systems and the stage raster sampling mode are novel within ion intensity versus fluence studies and provide an opportunity to better understand differences between simple and complex analyte systems and the optimal conditions for imaging studies. In addition, the dimensions of the in-source and the out-of-source laser beam profiles resulting from each fiber are recorded and analyzed. The nature of the beam profile features resulting from each fiber are assessed and the relation of certain features to the mass spectral data discussed. Subsequent recommendations for optimal beam profile photon distribution are provided.

Materials and Methods

Methanol (LC-MS grade) was purchased from Fisher Scientific (Leicestershire, UK). The water used was purified by an ELGA Purelab Option system (Marlow, UK). Trifluoroacetic acid (TFA; >99.9%) was purchased from Acros Organics (Loughborough, UK) and MALDI matrix α-cyano-4-hydroxycinnamic acid (CHCA) was purchased from Sigma Aldrich (>98%; Sigma-Aldrich, Dorset, UK). Lipid standard phosphatidylcholine (PC) 16:0/18:1 was purchased from Avanti Polar Lipids (Delfzyl, The Netherlands).

Sample Preparation

Thin film CHCA (10 mg/mL in 80% methanol 0.2% TFA) and lipid (0.04 mg/mL in 80% methanol) standard samples were prepared by premixing in a ratio of 1:1 (V:V) and spraying onto a stainless steel MALDI imaging target plate (Sciex, Concord, ON, Canada) using a TM Sprayer (HTX Technologies, LLC, Chapel Hill, NC, USA). For tissue imaging, 10-μm thick serial coronal sections were thaw mounted onto the same target plate (eight per MALDI plate, one plate was used for data acquisition with each optic fiber on consecutive days). CHCA (5 mg/mL in 80% methanol, 0.1% TFA) was sprayed onto these samples

also using the TM sprayer (full protocol in Supporting Information (SI) Section 1).

Optics Setup, Laser Energy Monitoring, and Beam Profiling

A Nd:YVO_4 laser (SPOT-0-100-355; Elforlight Ltd., Daventry, UK) was triggered from the QSTAR XL instrument (Sciex) using the existing TTL trigger signal in conjunction with a function generator (TTi – TG2000 20MHz DDS) triggering the laser at a repetition rate of 4 kHz. The laser was focused into either a 100 µm (4 m Fiberguide Industries via AMS Technologies, Leicestershire, UK), or 50 µm circular core optic fiber (3 m; Oz Optics, Ontario, Canada) or a 100 or 50 µm square core optic fiber (2 m; Fujikura Europe Ltd., Surrey, UK). The oMALDI II ion source optics focus the beam 1:1 onto the sample surface at an incidence angle of approximately 65°. Consequently the irradiated area on the sample surface is an elliptical or rectangular shape where circular or square core fibers are used. In-source beam profiles were acquired using a modified version of the fluorometric method [15]. Briefly, the laser attenuation was minimized so no ablation or modification of the CHCA matrix layer to one side of the sample plate was observed. Then an optical image of the fluorescence emitted from the matrix was acquired and used to estimate the size of the irradiated area by comparison to a feature of known size, in this case an image of a TEM grid attached to the sample plate. Further details can be found in the SI Section 2. The out-of-source laser beam profiling was carried out by uncoupling the fiber optic patchcord from the QSTAR and focusing it onto the CCD of a laser beam profiling camera (BGS-USB-SP620; Ophir Photonics, Darmstadt, Germany) with a ~10× magnification. The laser energy monitoring calibration was performed prior to the acquisition of each fiber's data set. These values were used to calibrate the on-line energy measures from the beam sampling mirror back to an estimate of the true on-sample incident laser energy. The optics setup used to control and monitor the laser beam energy as well as the fiber energy calibration data is described further within the SI Sections 1, 2, and 3.

Mass Spectrometry

Mass spectrometric analysis was carried out in continuous raster sampling imaging mode on a QSTAR XL Qq-ToF mass spectrometer fitted with an oMALDI II ion source (Sciex). Data acquisition from lipid standard thin layer preparations was performed by acquiring one single line raster of ~2 cm length for each laser energy setting. The pixel size in the x-dimension was set to 100 µm, resulting in ~200 spectra per energy setting. The stage was rastered at a speed of ~ 0.5 mm/s (the 'slow' setting in the oMALDI software). The raster line spacing was set to 280 µm to ensure no overlap (oversampling) of the consecutive raster line sampling regions. Tissue imaging data acquisition was carried out in the same manner but rather that one raster line per sample, the energy was kept constant for an image of one brain hemisphere for each of the eight tissue sections per plate (i.e., eight energies were investigated per fiber). Control images were acquired on the corresponding hemispheres of all tissue sections at a fixed energy. All data acquisition was carried out in the continuous raster sampling mode [16]. Images were acquired in a randomized order (SI Figure S1). Appropriate caution should be taken when handling dangerous chemicals and lasers.

Data Processing

The proprietary .wiff data files were converted to mzML using AB MS Data Converter ver. 1.3 (AB Sciex). These mzML files were then converted to imzML using imzMLConverter [17] and processed in custom-made software within MATLAB (ver. R2014b, MathWorks Inc., Natick, MA, USA). Data were then extracted and processed with standard MATLAB functionality. All reported ion intensities are integrated under the full area of the relevant peak. Mean ion intensities were calculated by producing mean spectra from user-selected on-tissue image regions, the integrated peak areas from these mean spectra were then calculated, and are reported below. Beam profile analysis was carried out in ImageJ, further details in SI Section 1, 2, and 3.

Results

Optic Fiber Core Shape and Laser Beam Profiling

The core shapes and laser beam profiles used in this study are shown in Figure 1. The dimensions of the irradiated region on the sample within the ion source were measured by the fluorometric method [15], taking advantage of the fluorescence

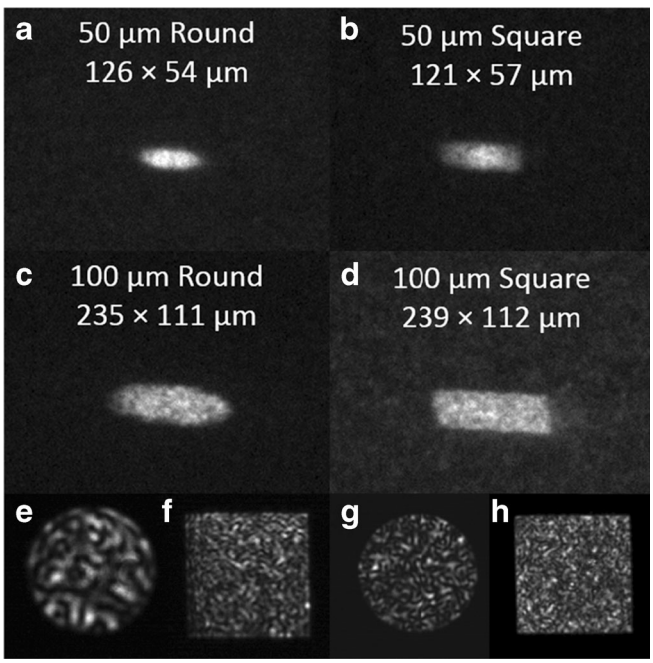

Figure 1. Example in-source fluorometric beam profile images from CHCA with accompanying dimension measurements (**a**–**d**) and out-of-source CCD beam profile images from 50 µm round, 50 µm square, 100 µm round, and 100 µm square core optic fibers (**e**–**h**), respectively

emission of CHCA. Additionally, out of source laser beam profile images were acquired to enable further analysis of their properties in relation to the mass spectrometric data (example images shown in Figure 1e–h).

The desire for novel-shaped beam profiles largely exists for two reasons. First, study of beam profiles with varying characteristics, such as shape, presents an interesting and potentially powerful route for fundamentals studies in MALDI MS. Second, the ability to ablate square regions is of interest in MALDI MSI, as there may be scope for improved sensitivity if all matrixes are ablated from within the (typically) square pixel region. The rectangular nature of the irradiated area on the sample plate resulting from the use of the square core fibers is clear.

Beam profile images were acquired for each fiber in triplicate where each image (single examples shown in Figure 1) was acquired with the fiber coiled in a different manner, giving a different speckle pattern. These beam profile images are the summation of approximately 1000 pulses. The beam profiles acquired in this fashion are stable, where the fiber is held still, but do vary to some extent around this average (data not shown). A threshold was applied to each beam profile image whereby all pixels below it were given the intensity value 0 and all above 1. The threshold values corresponding to a percentage of the total image intensity were applied and from the subsequent binary image the percentage area above this threshold, within the total irradiated area, was calculated. Example images resulting from this threshold process are shown in Figure 2b, c, and d. When applied to all acquired beam profile images over the full range of threshold intensity, the graph Figure 2e was created. The three beam profiles from each fiber group demonstrate well the characteristic photon distributions resulting from each fiber despite changes in speckle pattern stemming from different fiber positioning. The two 50 μm and two 100 μm core diameter fibers group together whereby the 50 μm fibers have a larger percentage of total intensity spread over a given percentage of the irradiated region. Further to this, the square fibers of either size have a greater percentage of their area occupied by pixels of a lower percentage of total energy compared with the corresponding size round fibers (i.e., the maxima within the square fiber photon distributions occupy a smaller portion of the irradiated area than those of the round fibers of equivalent diameter).

The consequence of these differences in beam profile as related to the size and number of beam profile features was also investigated. ImageJ was used to count and size features within the 4% area binary images for all beam profile images acquired (Figure 3).

This graph shows that the 50 μm round fiber has the fewest number of features, whereas the 100 μm square fiber has the largest number with both square fiber beam profiles having more features than their corresponding size round fibers. However, in the case of the square fibers, this larger number of features corresponds to a much smaller mean feature size, as a percentage of the total area, compared with the corresponding size round fiber beam profiles. The implications of these analyses are further discussed within the context of the corresponding mass spectrometric results below.

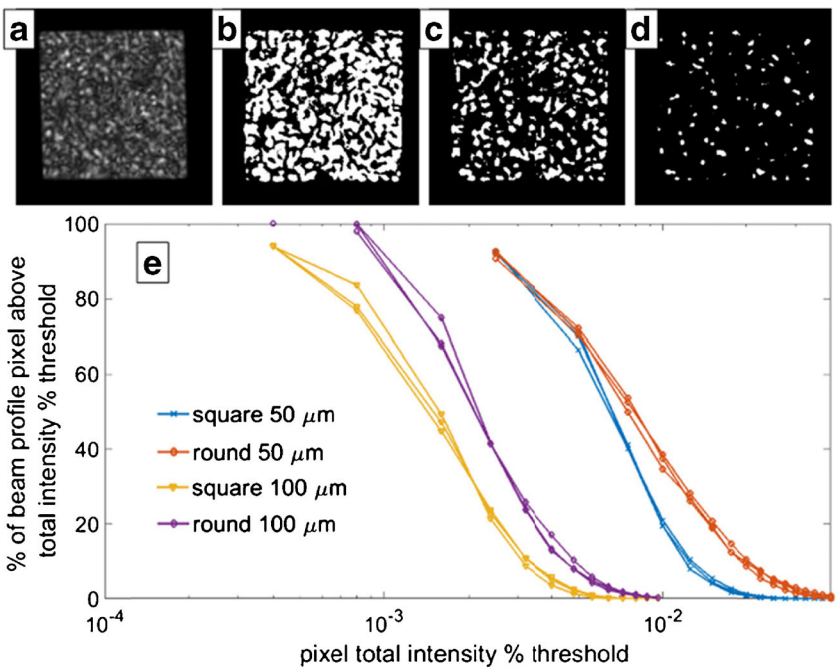

Figure 2. Beam profile image analysis for 50 and 100 μm square and round fibers. (**a**) Example CCD beam profile from 100 μm square fiber. (**b**–**d**) thresholds of beam profile at 1.6×10^{-3}, 2.4×10^{-3} and 3.9×10^{-3}% of total image intensity which correspond to areas containing 49, 21 and 4% of pixels within the beam profile, respectively. (**e**) Graph showing % of beam profile area above total % image intensity threshold for laser beam profiles resulting from the use of each fiber analyzed in triplicate

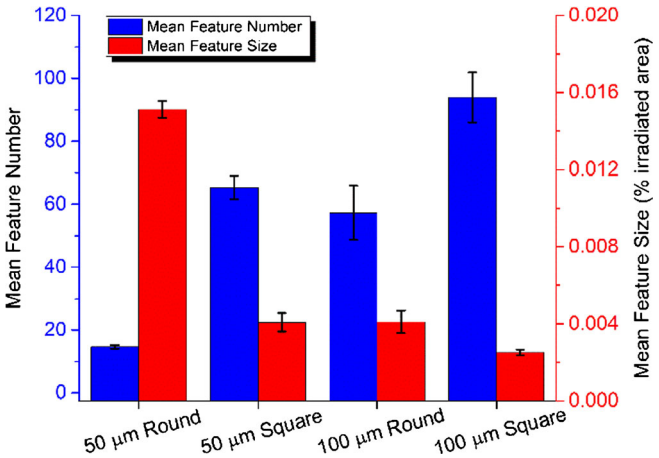

Figure 3. Mean feature number and feature size (as % of irradiated area) from 4% threshold beam profiles, an example of which is shown in Figure 2e. Speckle pattern intensity maxima for each fiber are summarized. The square core fibers show a larger number of smaller speckle maxima as compared with the same core diameter round fiber

Detected Ion Intensity versus Fluence for Different Fiber Optic Core Shapes

CHCA and PC 16:0/18:1 lipid standard thin layer preparations and CHCA coated murine brain sections were analyzed over a range of laser energies for each fiber optic patchcord. The left hemisphere of each coronal section was analyzed at a fixed energy to act as control and a different energy was employed for imaging each of the right hemispheres. Graphs showing ion intensity versus fluence (I versus F) for PC 34:1 $[M + H]^+$ at *m/z* 760.6 (for thin film) and PC 34:1 $[M + K]^+$ at *m/z* 798.5 (for tissue, tentatively assigned from literature [18–21]), for each fiber optic patchcord employed, are shown in Figure 4. These

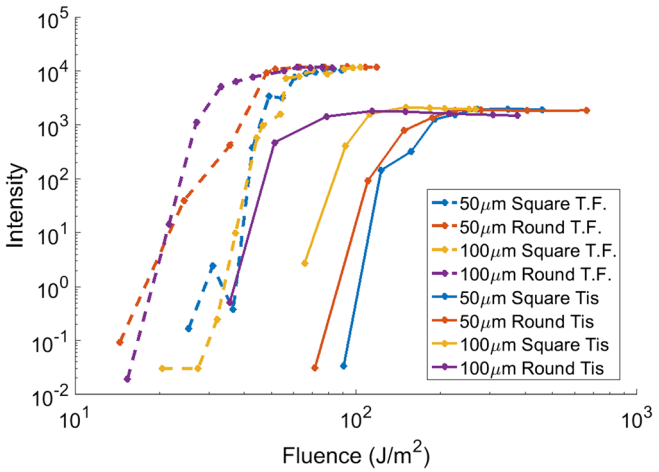

Figure 4. Detected ion intensity versus fluence from thin film CHCA and PC 34:1 lipid standard or CHCA and tissue obtained with either a 50 or 100 µm square or round fiber optic patchcord. Mean peak areas of ion PC 34:1 $[M + H]^+$ at *m/z* 760.6 (thin film) or PC 34:1 $[M + K]^+$ at *m/z* 798.5 (on-tissue). These are the most abundant adducts of PC 34:1 seen in these two respective systems

data are also shown for ion intensity versus laser energy within SI Figures S2 and S3. The peaks detected at *m/z* 760.6 and 798.5 were chosen for display as they are the dominant adduct ion detected for the same lipid within the respective systems. An example set of images from the on-tissue data is shown in Figure 5. The control (constant energy) and variable energy images obtained with each of the four patchcords for the ion at *m/z* 826.6 (tentatively assigned from literature as PC 18:0/18:1 $[M + K]^+$ [19–21]) and *m/z* 798.5 are displayed. Further images for *m/z* 184.1 (tentatively assigned from literature as PC head-group fragment $[C_5H_{14}NNaO_4P]$ [22, 23]) are displayed within SI Figure S4.

The I versus F curves shown within Figure 4 all have the similar general trends to those observed from peptides within the literature [2, 7, 9] whereby the low fluence data do not feature any detected ions, then as the fluence is increased past threshold, a steep rise in detected ion intensity is observed. For the single ion data, the curves then plateau soon after this initial increase and may even decrease again as fluence increases, whereas the TIC curves typically continue to increase to the maximum fluence, though the rate of increase is seen to drop off at the higher fluences, particularly for the 50 µm round fiber data (SI Figure S5). In all cases, the threshold fluence for ion detection and the I versus F curve plateau is lower for the thin film compared with the tissue for a given fiber (estimated values from single ion data for threshold fluence and I versus F plateau are shown in Table 1). For example, the round 100 µm fiber has the lowest threshold fluence in both thin film and tissue of ~24 and ~38 J/m^2 respectively. Conversely, the square 50 µm fiber gives rise to the largest threshold fluence in both sample types of ~40 and ~100 J/m^2. The square 50 µm fiber also plateaus at the highest fluence in thin film (~72 J/m^2) and tissue (~270 J/m^2) but conversely to the threshold fluence values, the round 50 µm fiber shows the lowest plateau fluence (~58 J/m^2) in thin film but not in tissue, where the 100 µm fiber also has the lowest plateau fluence (~114 J/m^2). One particularly interesting feature regarding these trends is that for the thin film data the 100 µm fibers have the largest fluence increase between threshold and plateau (~37 J/m^2 and ~42 J/m^2 for round and square, respectively), whereas the tissue data shows the opposite trend, whereby the 50 µm fibers show the largest fluence increase between threshold and plateau (~127 J/m^2 and ~170 J/m^2 for round and square, respectively). The order of threshold fluence value for thin film data is round 100 µm < round 50 µm < square 100 µm ≤ square 50 µm and for tissue data is round 100 µm < square 100 µm < round 50 µm ≤ square 50 µm. This ordering of ion detection threshold fluence only partially agrees with the observation by Ingendoh et al. that the smaller the focal diameter, the larger the threshold fluence observed [1]. It may be that other factors such as the beam profiles resulting from the square fibers compared with round fibers or the continuous raster mode sampling used within this study are also significant.

Whilst there are no I versus F studies in the literature employing lipids as the analyte, there are a few studies of this nature employing CHCA as the matrix. Qiao et al. [2] found ion detection fluence values of ~150 J/m^2 and ~200 J/m^2 and

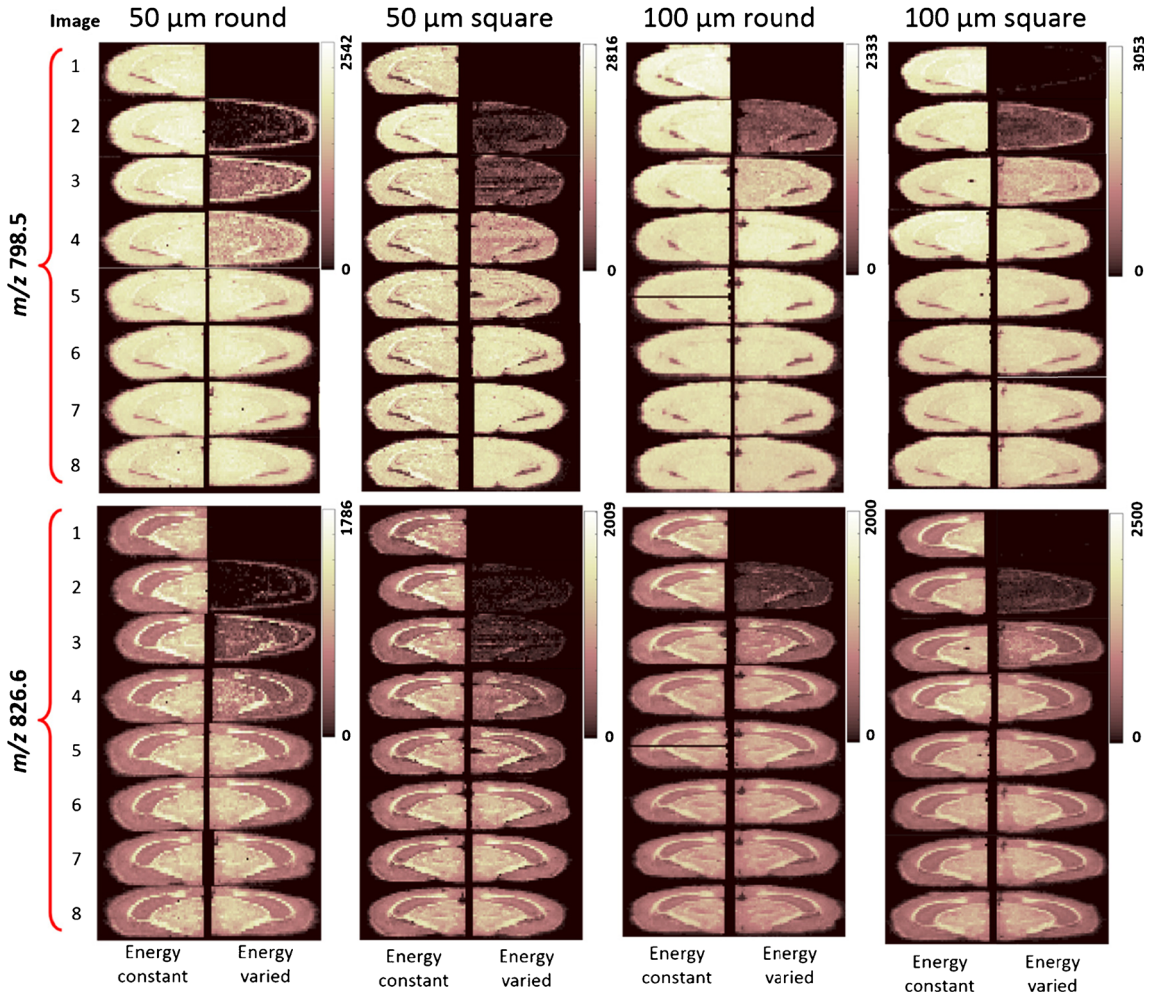

Figure 5. Single ion images from all tissue data sets for *m/z* 826.6 and 798.5. Images numbering 1 through 8 correspond to the fluence values shown in the I versus F curves within Figure 4 for tissue data. Increasing ion intensity can also be seen to tally with an improvement in image quality and changes in contrast between certain anatomic regions

plateau fluence values of ~200 J/m^2 and ~300 J/m^2 for round 100 µm and 50 µm core diameter fibers, respectively. Westmacott et al. recorded the I versus F response using 200 µm core fibers and found threshold fluence values of between ~12 and ~50 J/m^2 and plateau fluences of between ~30 and ~90 J/m^2 depending upon the ion detection setup employed [24]. Wiegelmann et al. found a threshold of ion production at ~30 J/m^2 and a plateau at ~110 J/m^2 when employing a 200 µm core diameter optic fiber [25]. Of these reported values, the data presented by Westmacott et al. and Wiegelmann et al. have most in common with the thin film data acquired here, despite using a fiber with twice the core diameter of the largest fiber within this study, whilst the trends shown in the study by Qiao et al. showed higher (up to

Table 1. Ion Detection Threshold Fluence (J/m^2) Values and the Fluence Value at Which the I Versus F Curves Plateau as Estimated from the Single Ion Data Graphs within Figure 2

	50 µm Round	50 µm Square	100 µm Round	100 µm Square
Thin Film – beam area	6688 µm^2	13878 µm^2	23288 µm^2	25949 µm^2
Thin film threshold	34	40	24	38
Thin film plateau	58	72	61	70
Difference	24	32	37	42
On-tissue – beam area	5865 µm^2	9260 µm^2	19104 µm^2	26317 µm^2
Tissue threshold	98	100	38	73
Tissue plateau	225	270	114	151
Difference	127	170	76	79
Thin film versus tissue threshold fluence difference	64	60	14	35
Thin film versus tissue plateau fluence difference	167	198	53	81

approximately six times) threshold and plateau values than even the on-tissue data presented here, with the same diameter fibers. It is not clear whether these differences are analyte-dependent or are due to some other factor such as the imprecise estimation of beam profile dimensions involved in calculating fluence or differing sample preparation methods.

Example optical images of ablated tracks following the on tissue data acquisition are presented in SI Figures S6–S9. Within these images, it is clear that for the 100 µm fibers the maximum amount of ablation is reached at a higher fluence than the corresponding plateau within the I versus F trends (Figure 4). This suggests that the ablation of the final additional material does not significantly add to the detected intact analyte ion intensity where near-complete ablation is achieved.

Image and Spectral Quality at Varying Fluence in MALDI MSI

The on-tissue data described above was acquired in imaging mode, and image of ions detected at *m/z* 798.5 and 826.6 are shown in Figure 5.

Image numbers shown within Figure 5 indicate which data points within Figure 4 the images correspond to where image 1 corresponds to the lowest fluence data point, image 2 to the next highest fluence data point, and so on. The laser energy used to acquire the control data are ~311, 364, 200, and 177 J/m^{-2} for the round 50 µm, square 50 µm, round 100 µm, and square 100 µm fibers, respectively. The increase in ion intensity seen within the single ion trends (Figure 4) are reflected in the improving quality of the images shown in Figure 5 until a certain energy where no further improvement in image quality is observed. This point is in clear synchronicity with the fluence at which the I versus F trends in Figure 4 first plateau (values also shown in Table 1).

Further to viewing the single ion intensities and associated images, viewing some of the mean on-tissue mass spectra reveal interesting features within these data. Several example mean spectra are shown in Figure 6.

The fluence at which the I versus F trends plateau vary but, significantly, the mean spectra from the initial plateau fluence for each fiber are very similar. Example spectra from the initial plateau of the 50 µm square and 100 µm round data are shown in Figure 6 A and B. Similar ion intensities across all peaks are observed despite the very different beam profiles, laser energies, and areas irradiated within each experiment. Additionally, the impact of fluence over the ranges investigated is exemplified by the spectra shown in Figure 6C and D. Here the lower energy shows little to no ions below ~*m/z* 700, which would typically feature lipid fragments and matrix-related ions for this type of analysis. In contrast, the highest fluence investigated for the 50 µm round fiber shows higher intensity for intact lipid species within the *m/z* 700–900 region as well as considerable signal from lipid fragment ions and matrix-related ions. The PC lipid headgroup fragment at *m/z* 184.1 is more intense than the intact lipid ions.

Interestingly, the quality of the images in Figure 5 do not entirely reflect the apparent quality of the mean on-tissue spectra from their corresponding data. For example, the

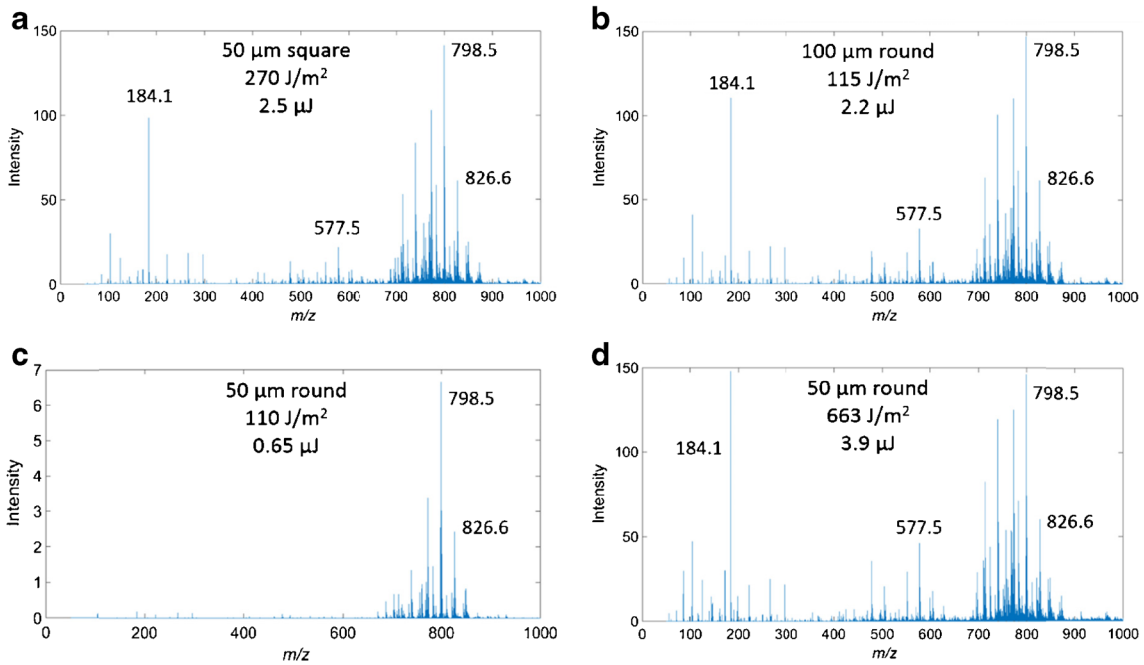

Figure 6. Example mean on-tissue spectra are shown for several of the image data sets shown above. The *m/z* value of pertinent peaks 184.1, 577.5, 798.5, and 826.6 (lipid headgroup fragment, lipid fragment, and two intact lipid ions, respectively) are labeled. Spectra A and B are from the points within the 50 µm square and 100 µm round data (respectively) at which the I versus F curves first plateau. Similar ion intensities are observed at these plateau points in all data sets. Spectra C and D show two fluence data points from the 50 µm round fiber images. Very different mean spectra are observed depending upon the fluence employed

spectrum corresponding to the round 50 μm image 2 at 110 J/m^2 (Figure 6C) in Figure 4 shows a reasonable number of peaks with high signal-to-noise ratio, albeit with a low peak intensity. Looking at such a spectrum in isolation would possibly lead one to conclude the data set was of reasonable quality, a conclusion which is immediately contradicted when one views the corresponding single ion image. This exemplifies the risk of relying on mean spectra from large tissue regions as being representative of good quality data.

Significantly, it can also be seen that the threshold fluence of ion generation does not occur at the same value across all areas of the tissue. For example, within image two (Figure 5, either ion) of the energy varied 50 μm round fiber data the edge of the tissue is clearly more intense than much of the central region, whereas in the higher energy images this is not the case. This same phenomenon of contrast between certain features changing as the fluence is increased is also visible for tissue subregions. Furthermore, the level of fragmentation, as measured by the intensity of the ion at *m/z* 184.1, is also seen to vary across different areas of the tissue and between the different fiber data sets (SI Figures S4, S10, and S11). These tissue region-specific issues were studied further by plotting I versus F data from mean spectra derived from specific anatomic subregions of the 100 μm square fiber data as roughly guided by the Allen Brain Atlas (example anatomic region shown in SI Figure S12). Most pertinently, relative detected ion intensities between different tissue sub-regions vary depending upon the fluence employed. For example, the mean ion intensity for *m/z* 798.5 within the approximate thalamus region (SI Figure S13) is the least intense of the regions investigated at 92 J/m^2, whereas at 151 J/m^2 fluence, it is the second most intense region. Similar variation in relative contrast between low and higher fluence are shown for the TIC as well as the ions at *m/z* 826.6 and 184.1 (SI Figures S14–S16, respectively).

Discussion

The differing fluence threshold values for each fiber and the corresponding plateau values show that the round 100 μm fiber is likely to give the best performance at low fluences, particularly within the on-tissue data. Interestingly, there is relatively little difference between the maximum detected ion intensities for each of the fibers (Figure 4). These data were all acquired in continuous raster mode whereby the stage is moved continuously under the laser and the data is delineated into pixels by a time period that is calculated from the desired pixel width and the speed of the stage. Therefore, where no oversampling [26] is employed between each row of pixels (as in this study), the size of each pixel in this vertical dimension is dictated by the height of the irradiated region. Optical images of the sample after analysis, showing material removal, are shown in SI Figures S6–S9. Consequently, the major axis of each beam profile dictates the size of this dimension and it follows that the 50 μm fibers result in approximately twice the detected ion intensity from a given area compared with the 100 μm fibers. This is shown explicitly within SI Figures S17 and S18 where the ion intensity values are normalized to the height of the irradiated area for the thin film and tissue data, respectively.

Comparison of the beam profile analyses and the corresponding MSI data for varying fluence suggest that the for a fiber of a given diameter, the larger the amount of energy shared over a given area of the beam profile, the lower the threshold energy that will be observed (Figure 2). This correlates with fewer but larger features within the beam profile (Figure 3) for fibers of each diameter. Where the ion intensity versus laser energy is considered, there is also correlation to these characteristics where the 50 μm round fiber shows the lowest threshold energy and the 100 μm square fiber shows the largest, possibly also suggesting a benefit from photon distributions with fewer larger speckle features.

The qualitative demonstration of correlation between the single ion I versus F curve shape and corresponding image quality presents new context to MALDI MSI studies. Additionally, a number of image features shown in Figure 5 and SI Figure S4 provide additional information, highlighting an important reason to perform these studies in an imaging, rather than tissue profiling, mode. The spatial variation of the ion detection threshold within these images demonstrates two interrelated points: a fluence-related perspective to such concepts as tissue type-specific ion suppression and an illustration of the difference between thin film and on-tissue ion production/detection. Quantitation within tissue imaging studies has recently been refined in an attempt to account for tissue type-specific changes in ion suppression [27]. It can be imagined that adjustment of fluence during MALDI MSI for tissue region-specific I versus F response could, in the future, be employed, either in a reactive on-line adjustment similar to the work of the Kim group [28] or as a predetermined adjustment based on prior knowledge of the tissues being analyzed, thus potentially negating the need for or enhancing the impact of post-acquisition data normalization strategies.

Curve fitting to the aforementioned power law function was performed for these data and m values are shown in SI Table S1. These values range from 1.4 to 6.3 and though some weak trends are present, such as square fibers showing larger m values than the corresponding size round fibers, for the single ion data, the m values do not appear to be a more useful descriptor of our data than the threshold and plateau fluence values shown in Table 1. Recently, Soltwisch et al. [7] published a new sigmoidal fitting function for their I versus F data where some of the parameters were approximations of physical variables, such as threshold fluence, as opposed to only being empirical fitting parameters. Their function was also applied as a curve fit for the data within this article but issues with overfitting of the data and subsequent poor fitting were encountered. Therefore, we have chosen only to report the more traditional power law fitting.

An increase in laser energy in laser desorption/ablation-type studies can lead to an increase in fragmentation of ejected molecules [2, 7, 9]. Within this study, an increase in fragmentation (monitored by proxy with the lipid headgroup fragment

peak at *m/z* 184.1 and PC lipid sidechain loss fragment at *m/z* 577.5, data not shown) was observed with increasing fluence in absolute terms as well as relative to the intensity of the fragment's parent molecule and to the TIC. This phenomenon was also evident in the tissue image of the fragment ion at *m/z* 184.1 (SI Figure S4). Interestingly, the ratio of detected fragment to parent-ion levels out and remains constant at higher fluences, implying that the addition of further energy into the system does not lead to significant further fragmentation. Perhaps additional fragmentation occurs via different pathways, requiring a higher energy of activation, leading to the emergence of other lower intensity peaks throughout the spectrum.

There also appears to be a change in the ratio of intact lipid adducts, $[M + H]^+$ and $[M + Na]^+$, at *m/z* 760.6 and 782.6, within the thin film data, as the fluence is increased (SI Figure S19). These changing peak intensity ratios level out at higher fluences, which may suggest the realization of a stoichiometric sharing of charge is reached at higher fluence, perhaps due to increased collisions in a hotter or denser plume.

These changing spectral properties, in addition to the I versus F trend for single ions of interest, should be taken into account when carrying out MALDI MSI experiments. Therefore, knowledge of the I versus F relationships for the particular system under investigation is important for a more complete understanding of the detected intensity measured. In addition, changing peak ratios may show that detected ion intensity variation with fluence cannot simply be normalized away with a single normalization factor accounting for all ions within the spectra.

Conclusions

For the first time, the relationship between laser fluence and detected ion intensity in MALDI MS was investigated with lipid as the chosen analyte and, significantly, within a tissue imaging context. Round fibers are recommended for general use and tissue imaging applications over square fibers, and a smaller core diameter fiber is likely to provide a lower energy requirement and higher sensitivity per interrogated area. However, smaller fibers may damage more easily because of the need to focus the laser energy onto a smaller area, resulting in a higher energy density on the fiber core face. The quality of images acquired with each fiber is similar but the fluence at which an image is acquired will have a big impact upon image quality. The highest quality images with the lowest amount of associated lipid fragmentation are acquired at a fluence 20–45% higher than the point at which the I versus F trend first plateaus, depending upon the fiber in question, a region which, for tissue, is approximately three times the threshold fluence observed. In addition, this study demonstrates that MALDI MSI should be carried out at known energies as the contrast between different tissue sub-regions may have some dependence upon the fluence used.

The beam profile analyses within this study, viewed alongside the I versus F data, suggest that the characteristics displayed by the round fibers are more desirable than those of the square core fibers. Therefore, a beam profile with a smaller number of speckle pattern features that occupy a relatively large percentage of the irradiated area is recommended as likely to provide the highest sensitivity data. Thus, neither Gaussian nor flat top beam profiles are likely to be optimal, but some photon distribution between these two extremes. Additionally, the size, shape, and type of matrix crystals are likely to influence the nature of the optimal beam photon distribution for a given MALDI MS and MSI experiment.

Finally, study of the relationship between detected ion intensity and laser fluence have previously only been carried out in spot-to-spot sampling mode, often employing a 'random walk' at each location. Possible similarities or differences in the relationship of detected ion intensity and laser fluence between this sampling mode and continuous raster sampling have not been studied and would potentially be and interesting topic for future study.

Acknowledgments

The authors thank Alasdair Rae and Keith Oakes for useful discussion. Funding was provided by NPL strategic research program NiCE MSI (SR 116301) and Innovate UK (formerly TSB) award 101788.

References

1. Ingendoh, A., Karas, M., Hillenkamp, F., Giessmann, U.: Factors affecting the resolution in matrix-assisted laser desorption-ionization mass spectrometry. Int. J. Mass Spectrom. Ion Processes **131**, 345–354 (1994)
2. Qiao, H., Spicer, V., Ens, W.: The effect of laser profile, fluence, and spot size on sensitivity in orthogonal-injection matrix-assisted laser desorption/ionization time-of-flight mass spectrometry. Rapid Commun. Mass Spectrom **22**, 2779–2790 (2008)
3. Dreisewerd, K., Schurenberg, M., Karas, M., Hillenkamp, F.: Influence of the laser intensity and spot size on the desorption of molecules and ions in matrix-assisted laser-desorption ionization with a uniform beam profile. Int. J. Mass Spectrom **141**, 127–148 (1995)
4. Dreisewerd, K.: The desorption process in MALDI. Chem. Rev. **103**, 395–425 (2003)
5. Knochenmuss, R., Zhigilei, L.V.: Molecular dynamics simulations of MALDI: laser fluence and pulse width dependence of plume characteristics and consequences for matrix and analyte ionization. J. Mass Spectrom **45**, 333–346 (2010)
6. Guenther, S., Römpp, A., Kummer, W., Spengler, B.: AP-MALDI imaging of neuropeptides in mouse pituitary gland with 5 µm spatial resolution and high mass accuracy. Int. J. Mass Spectrom **305**, 228–237 (2011)
7. Soltwisch, J., Jaskolla, T.W., Dreisewerd, K.: Color matters—material ejection and ion yields in UV-MALDI mass spectrometry as a function of laser wavelength and laser fluence. J. Am. Soc. Mass Spectrom. **24**, 1477–1488 (2013)
8. Soltwisch, J., Jaskolla, T.W., Dreisewerd, K.: Erratum to: Color Matters—material ejection and ion yields in UV-MALDI mass spectrometry as a function of laser wavelength and laser fluence. J. Am. Soc. Mass Spectrom. **26**, 1641–1641 (2015)
9. Guenther, S., Koestler, M., Schulz, O., Spengler, B.: Laser spot size and laser power dependence of ion formation in high resolution MALDI imaging. Int. J. Mass Spectrom. **294**, 7–15 (2010)
10. Hsieh, Y., Casale, R., Fukuda, E., Chen, J., Knemeyer, I., Wingate, J., Morrison, R., Korfmacher, W.: Matrix-assisted laser desorption/ionization imaging mass spectrometry for direct measurement of clozapine in rat brain tissue. Rapid Commun. Mass Spectrom. **20**, 965–972 (2006)

11. Lagarrigue, M., Becker, M., Lavigne, R., Deininger, S.-O., Walch, A., Aubry, F., Suckau, D., Pineau, C.: Revisiting rat spermatogenesis with MALDI imaging at 20-μm resolution. Mol. Cell. Proteom. **10**, M110. 005991 (2011)
12. Milasinovic, S., Liu, Y., Bhardwaj, C., Blaze, M.T., Gordon, M.R.J., Hanley, L.: Feasibility of depth profiling of animal tissue by ultrashort pulse laser ablation. Anal. Chem. **84**, 3945–3951 (2012)
13. Holle, A., Haase, A., Kayser, M., Hohndorf, J.: Optimizing UV laser focus profiles for improved MALDI performance. J. Mass Spectrom. **41**, 705–716 (2006)
14. Sherrod, S.D., Castellana, E.T., McLean, J.A., Russell, D.H.: Spatially dynamic laser patterning using advanced optics for imaging matrix assisted laser desorption/ionization (MALDI) mass spectrometry. Int. J. Mass Spectrom. **262**, 256–262 (2007)
15. Steven, R.T., Palmer, A.D., Bunch, J.: Fluorometric Beam Profiling of UV MALDI Lasers. J. Am. Soc. Mass Spectrom. **24**, 1146–1152 (2013)
16. Race, A.M., Styles, I.B., Bunch, J.: Inclusive sharing of mass spectrometry imaging data requires a converter for all. J. Proteom. **75**, 5111–5112 (2012)
17. Jackson, S.N., Ugarov, M., Post, J.D., Egan, T., Langlais, D., Schultz, J.A., Woods, A.S.: A study of phospholipids by ion mobility TOFMS. J. Am. Soc. Mass Spectrom. **19**, 1655–1662 (2008)
18. Wang, H.Y.J., Liu, C.B., Wu, H.W., Kuo, J.S.: Direct profiling of phospholipids and lysophospholipids in rat brain sections after ischemic stroke. Rapid Commun. Mass Spectrom. **24**, 2057–2064 (2010)
19. Steven, R.T., Race, A.M., Bunch, J.: Para-nitroaniline is a promising matrix for MALDI-MS imaging on intermediate pressure MS systems. J. Am. Soc. Mass Spectrom. **24**, 801–804 (2013)
20. Shrivas, K., Hayasaka, T., Goto-Inoue, N., Sugiura, Y., Zaima, N., Setou, M.: Ionic matrix for enhanced MALDI imaging mass spectrometry for identification of phospholipids in mouse liver and cerebellum tissue sections. Anal. Chem. **82**, 8800–8806 (2010)
21. Zemski Berry, K.A., Hankin, J.A., Barkley, R.M., Spraggins, J.M., Caprioli, R.M., Murphy, R.C.: MALDI imaging of lipid biochemistry in tissues by mass spectrometry. Chem. Rev. **111**, 6491–6512 (2011)
22. Wang, X., Han, J., Chou, A., Yang, J., Pan, J., Borchers, C.H.: Hydroxyflavones as a new family of matrices for MALDI tissue imaging. Anal. Chem. **85**, 7566–7573 (2013)
23. Westmacott, G., Ens, W., Hillenkamp, F., Dreisewerd, K., Schurenberg, M.: The influence of laser fluence on ion yield in matrix-assisted laser desorption ionization mass spectrometry. Int. J. Mass Spectrom. **221**, 67–81 (2002)
24. Jurchen, J.C., Rubakhin, S.S., Sweedler, J.V.: MALDI-MS imaging of features smaller than the size of the laser beam. J. Am. Soc. Mass Spectrom. **16**, 1654–1659 (2005)
25. Wiegelmann, M., Soltwisch, J., Jaskolla, T.W., Dreisewerd, K.: Matching the laser wavelength to the absorption properties of matrices increases the ion yield in UV-MALDI mass spectrometry. Anal. Bioanal. Chem. **405**, 6925–6932 (2013)
26. Hamm, G., Bonnel, D., Legouffe, R., Pamelard, F., Delbos, J.-M., Bouzom, F., Stauber, J.: Quantitative mass spectrometry imaging of propranolol and olanzapine using tissue extinction calculation as normalization factor. J. Proteom. **75**, 4952–4961 (2012)
27. Ahn, S.H., Kang, J.W., Moon, J.H., Kim, K.P., Lee, S.H., Kim, M.S.: Quick quantification of proteins by MALDI. J. Mass Spectrom. **50**, 596–602 (2015)
28. Bae, Y.J., Park, K.M., Kim, M.S.: Reproducibility of temperature-selected mass spectra in matrix-assisted laser desorption ionization of peptides. Anal. Chem. **84**, 7107–7111 (2012)